Joule

Article

Suppressing defects in kesterite solar cells via balanced phase evolution to enable 15.1% certified record efficiency

Graphical abstract

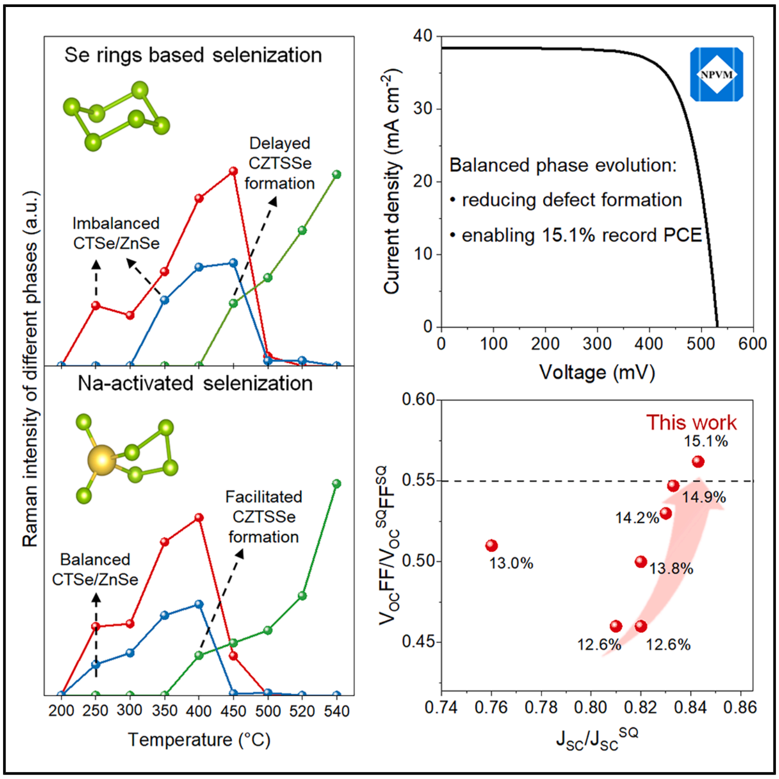

Highlights

- Kinetics-linked origin of Zn-related defects identified during CZTSSe selenization
- Na-Se$_x$ activation accelerates Cu_2SnSe_3 formation and balances phase evolution
- Synergistic phase evolution suppresses Sn_{Zn} and Cu_{Zn} defect generation
- 15.1% certified CZTSSe efficiency clears a key commercialization benchmark

Authors

Menghan Jiao, Bowen Zhang, Jinlin Wang, ..., Yanhong Luo, Dongmei Li, Qingbo Meng

Correspondence

shijj@iphy.ac.cn (J.S.),
qbmeng@iphy.ac.cn (Q.M.)

In brief

Kesterite (CZTSSe) solar cells use earth-abundant, non-toxic elements but their efficiency is limited by complex defects. We show that an imbalance between intermediate phases during selenization triggers harmful Zn-related defects. Introducing reactive Na-Se$_x$ species accelerates Cu_2SnSe_3 formation and balances phase evolution into CZTSSe, suppressing defect formation. This kinetic control enables a certified 15.1% device performance, clearing a key commercialization benchmark for sustainable thin-film photovoltaics.

Jiao et al., 2026, Joule *10*, 102345

https://doi.org/10.1016/j.joule.2026.102345

CellPress

Please cite this article in press as: Jiao et al., Suppressing defects in kesterite solar cells via balanced phase evolution to enable 15.1% certified record efficiency, Joule (2026), https://doi.org/10.1016/j.joule.2026.102345

Joule

CellPress

Article

Suppressing defects in kesterite solar cells via balanced phase evolution to enable 15.1% certified record efficiency

Menghan Jiao,[1,2,6] Bowen Zhang,[1,2,6] Jinlin Wang,[1,6] Xiao Xu,[1,6] Tan Guo,[1,3] Shudan Chen,[1,2] Jingchen Wang,[1,2] Yuan Li,[1] Yiming Li,[1] Huijue Wu,[1] Jiangjian Shi,[1,*] Yanhong Luo,[1,2,4] Dongmei Li,[1,2,4] and Qingbo Meng[1,2,4,5,7,*]

[1]Beijing National Laboratory for Condensed Matter Physics, Institute of Physics, Chinese Academy of Sciences, Renewable Energy Laboratory, Beijing 100190, P.R. China
[2]School of Physical Sciences, University of Chinese Academy of Sciences, Beijing 100049, P.R. China
[3]College of Materials Science and Optoelectronic Technology, University of Chinese Academy of Sciences, Beijing 100049, P.R. China
[4]Songshan Lake Materials Laboratory, Dongguan 523808, P.R. China
[5]Center of Materials Science and Optoelectronics Engineering, University of Chinese Academy of Sciences, Beijing 100049, P.R. China
[6]These authors contributed equally
[7]Lead contact
*Correspondence: shijj@iphy.ac.cn (J.S.), qbmeng@iphy.ac.cn (Q.M.)
https://doi.org/10.1016/j.joule.2026.102345

CONTEXT & SCALE As climate change intensifies, accelerating the transition to clean and scalable energy technologies is an urgent global priority. Thin-film photovoltaics are well suited for large-area, lightweight, and low-cost deployment, and kesterite $Cu_2ZnSn(S,Se)_4$ (CZTSSe) absorbers are uniquely attractive because they are composed entirely of earth-abundant and environmentally benign elements. In principle, kesterites could enable truly sustainable, terawatt-scale solar deployment, but their commercial viability has been fundamentally constrained by severe open-circuit voltage losses arising from complex defect chemistry. Here, we trace these defects to phase-evolution kinetics during selenization, revealing that delayed formation of Cu_2SnSe_3 relative to ZnSe creates an intermediate phase imbalance that induces Zn-substitution defect formation and enhances non-radiative recombination. Guided by this mechanistic insight, we develop a sodium-activated selenization strategy using reactive Na-Se_x species to accelerate Cu_2SnSe_3 formation and synchronize phase evolution toward single-phase CZTSSe. By suppressing harmful defect generation at its kinetic origin, this approach substantially reduces voltage loss and enables a certified 15.1% CZTSSe device efficiency. These results effectively address the central efficiency bottleneck in kesterite photovoltaics and mark a significant step toward the commercial viability of earth-abundant thin-film solar technology.

SUMMARY

Precise control of point defects is imperative for enhancing the performance of emerging kesterite solar cells, yet remains challenging in the multinary $Cu_2ZnSn(S,Se)_4$ (CZTSSe) due to its complex defect chemistry. Here, guided by the correlation between phase-evolution kinetics and defect formation, we identify that the delayed formation of Cu_2SnSe_3 (CTSe) relative to ZnSe during selenization promotes Zn-related antisite defects, including Sn_{Zn} and Cu_{Zn}. To rebalance these competing phases, we develop a sodium-activated selenization strategy by pre-constructing reactive Na-Se_x species and introducing them into the selenization process. This approach accelerates CTSe formation at lower temperatures, drives the synergistic ZnSe-CTSe transformation toward the CZTSSe phase, and effectively suppresses defect generation. Consequently, a certified power conversion efficiency of 15.1% is achieved with substantially reduced voltage loss, surpassing the commercialization threshold and opening opportunities for scalable inorganic photovoltaics.

INTRODUCTION

Precise control of point defects is crucial for enhancing photovoltaic device performance, especially for low-cost and eco-friendly emerging kesterite solar cells, whose photovoltaic efficiency has long been severely limited by the inherent complex and diverse point defects in multinary $Cu_2ZnSn(S,Se)_4$ (CZTSSe) light absorbers.[1–9] Understanding and regulating defects has been one

Please cite this article in press as: Jiao et al., Suppressing defects in kesterite solar cells via balanced phase evolution to enable 15.1% certified record efficiency, Joule (2026), https://doi.org/10.1016/j.joule.2026.102345

of the most challenging topics in the field of kesterite thin-film solar cells. Recent studies have increasingly indicated that antisite defects, Sn_{Zn} and Cu_{Zn}, are critical defects that cause charge loss in the cell, and moreover, that their formation is closely related to the complex reaction processes of CZTSSe selenization and crystallization.[10–17] In particular, insufficient elemental and lattice reconstruction during the transition from intermediate binary/ternary phases to the final CZTSSe is a critical reason inducing defect formation.[11,12,15–17] These findings highlight that the fundamental route to eliminating defects in CZTSSe lies in precisely controlling the microscopic processes involved in phase evolution.

Researchers have been dedicated to eliminating intermediate phases, especially Cu-Sn-rich phases, to realize the control of phase evolution and related defects.[10,11,18–26] For instance, Xin adjusted the valence states of precursor metal elements to avoid additional redox reactions during crystallization, thus suppressing the formation and evolution of Sn-selenide-related intermediate phases.[10,19] We developed high-pressure selenization and solid-liquid/solid-gas co-selenization strategies to adjust the Se vapor concentration in the reaction environment, effectively inhibiting the intermediate phases such as Cu_xSe and Cu_2SnSe_3 (CTSe).[24,25] Additionally, we introduced multi-element alloying strategies to modulate the atomic bonding states of intermediate phases, promoting their fusion reactions and reducing defect formation.[11] These efforts have raised the efficiency of CZTSSe solar cells to over 14%.

To further control defects effectively, we here revisited the phase evolution kinetics related to defect formation in CZTSSe, based on the Cu-Zn-Sn-Se thermodynamic phase diagram and the formation characteristics of metal selenides. We found that the spontaneously delayed formation of CTSe relative to ZnSe decreased the transformation reactivity of ZnSe to CZTSe, which could induce the generation of Zn-substitution-related defects (i.e., Sn_{Zn} and Cu_{Zn}). To overcome this challenge, we explored a sodium-activated selenization strategy to balance the evolution of CTSe and ZnSe phases. Specifically, we pre-constructed Na-Se_x species with exposed, active, non-cyclic selenium atoms and introduced them for selenization, which significantly facilitated the CTSe formation at lower temperatures and thus accelerated the synergistic evolution of CTSe and ZnSe toward CZTSSe. This reduced the sustained accumulation of ZnSe, thereby allowing more active Zn to participate in phase fusion reactions and inhibiting the formation of Zn-substitution-related defects. With these advantages, we achieved a certified power conversion efficiency (PCE) of 15.1% in CZTSSe solar cells with a significantly reduced open-circuit voltage (V_{OC}) loss. This achievement benefited from our proposed highly compatible experimental strategy, which has surpassed the commercialization threshold for this class of solar cells, thus paving the way for further development of emerging inorganic solar cells.

RESULTS AND DISCUSSION

Phase evolution processes correlated with defect formation

We first investigated key phase evolution processes influencing defect formation with the aid of the phase diagram of the Cu-Zn-Sn-Se system and the reaction equilibrium relationship of various metal selenide phases. We paid particular attention to the reaction pathway of Zn, as its substitution in CZTSSe is directly associated with the formation of detrimental defects. The phase diagram in Figure 1A indicates that in the multiphase evolution, the only pathway for Zn incorporation into the final CZTSe phase is through the reaction with CTSe, as Zn cannot form any ternary selenide phase with Cu or Sn (Figure S1). However, as shown in Figure 1B, the formation of the CTSe phase is much more difficult than that of ZnSe due to the requirement of higher temperature and Se vapor concentration,[16,24] implying that the CTSe phase forms later than ZnSe during selenization.

This delay behavior was proved in an experiment through investigating the selenization of precursors comprising different metal element components. As the Raman spectra show in Figure 1C and Figure S2, regardless of whether it was selenized alone or mixed with other elements, Zn can easily transform into ZnSe (with Raman peaks located at about 200 and 250 cm^{-1}) at a low temperature of 250°C.[27] In contrast, in the Cu-Sn system, the CTSe phase with a Raman peak located at about 180 cm^{-1} began to form only after 300°C.[28] In the Cu-Zn-Sn system, the existence of Zn further suppressed the CTSe phase, which did not appear until 350°C, while during this process, the ZnSe phase further strengthened. These results indicated that this delay allowed the initially formed nanoscale ZnSe phase to accumulate and grow. Apparently, this will decrease the Gibbs free energy of the ZnSe phase in the reaction system (Figure 1D) and thus influence the reactivity of ZnSe in combining with the subsequently appeared CTSe to transform to CZTSe, thereby resulting in the formation of defects related to Zn deficit and cation substitution, such as Sn_{Zn} and Cu_{Zn}, in the final CZTSSe. These findings highlight the necessity of accelerating the formation of the CTSe phase to achieve a balance with ZnSe, for sustaining the ZnSe/CTSe reaction system in a highly reactive state during the evolution toward the final CZTSSe.

Balancing phase evolution via activated selenization

Enhancing the reactivity of Se molecular reactants is a promising approach to facilitate an earlier achievement of the conditions required for CTSe formation in the reaction system. However, the regulation of selenium molecular species within the reaction system remains a significant challenge.[29–35] To address this, we here developed a sodium-activated selenization strategy, as schematically depicted in Figure 2A. Specifically, we pre-reacted Se with a Na source, for example, soda-lime glass (SLG), at high temperatures in a graphite box. The reaction products could adsorb in the graphite box, which was subsequently used for the selenization of CZTSSe samples.

Ab initio molecular dynamics (AIMD) simulations showed that in the pre-reaction system, Se_6 molecules can adsorb to the Na atom on the SLG surface through Na-Se interactions (Figure S4). These interactions gradually break the bond between Na and O and induce the formation of the Se_6-Na structure. In the Se_6-Na structure, the Na atom gradually inserts, forming a Se_6-Na ring, and continues to induce the reconstruction of the cyclic structure (Figure S5), ultimately evolving to the final molecular structure shown in Figure 2B. In this structure, two Se atoms are exposed and possess high electron density (Figure S6). When this

Please cite this article in press as: Jiao et al., Suppressing defects in kesterite solar cells via balanced phase evolution to enable 15.1% certified record efficiency, Joule (2026), https://doi.org/10.1016/j.joule.2026.102345

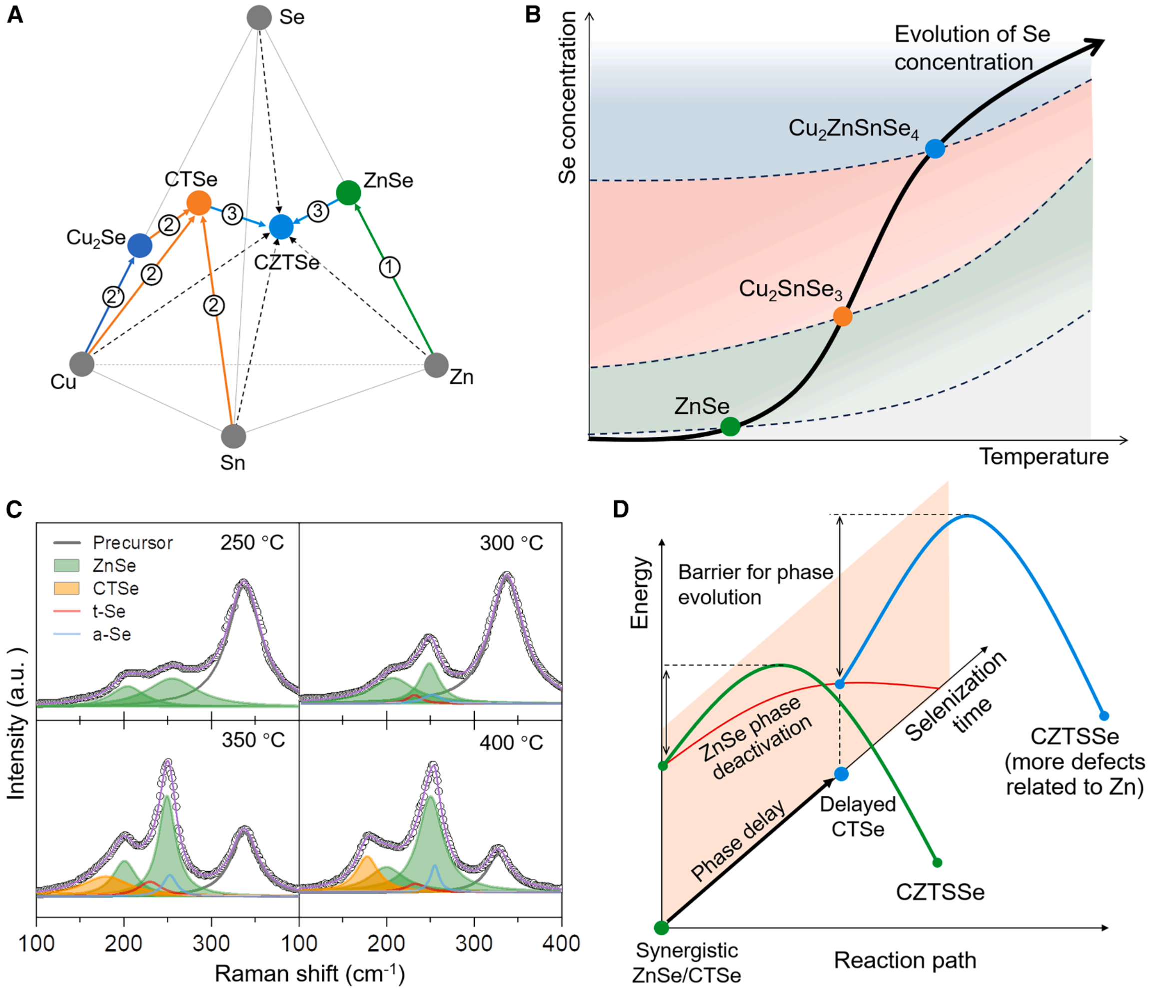

Figure 1. Correlation between unbalanced phase evolution and defect formation

(A and B) Schemes of (A) phase diagram of Cu-Zn-Sn-Se system and (B) the temperature-Se vapor equilibrium relationship governing the formation of metal selenides. In (A), the dashed arrow lines represent a direct combination reaction between Cu, Zn, Sn, and Se to form the CZTSe phase, and the solid arrow lines represent phase evolution from binary and ternary intermediate phases.

(C) Raman spectra (excitation at 325 nm) of Cu-Zn-Sn precursor films selenized at varied temperatures for 200 s. The spectra are fitted using multiple Lorentz-type peaks.

(D) Schematic diagram of energy evolution for the reaction system starting with different states of ZnSe phase in selenization. In the energy-selenization time coordinate plane, the decrease in energy represents the deactivation of the continuously grown ZnSe phase. The deactivation of ZnSe results in a higher energy barrier for the phase evolution, leading to the formation of more defects related to Zn substitution in the final CZTSSe. In contrast, the simultaneous emergence of CTSe and ZnSe phases can sustain the high reactivity of the system, thus suppressing the formation of related defects.

molecule is used as the selenium source, only ~0.5 eV is required to dissociate the exposed Se atoms to react with the Cu-Zn-Sn system (Figure 2C). This dissociation energy is only one-tenth of that of Se_6 (~5.2 eV) and is also significantly smaller than that of the Se_2 molecule (~2.8 eV). This suggests that we have obtained a Se species with much higher reactivity.

The construction of the Na-Se species was further demonstrated in an experiment. Raman spectra of the inner wall of the graphite box showed that the Na-Se pre-reaction obviously altered the vibrational characteristics of the adsorbed Se, manifested as broadening of the Raman peaks, a decrease in intensity, and a blueshift of the main peak (Figure 2D). This is because incorporation of Na leads to more diverse bond vibrations within the Na-Se complexes (Figure S7). Atomic emission spectroscopy measurements (Figure S8) revealed that Se significantly enhanced Na volatilization from the SLG, due to the reaction occurring between Se and Na.

When this Na-Se species was introduced into the selenization system, Raman investigations demonstrated that the formation of the CTSe phase was significantly accelerated, which had already appeared at 250°C (Figure 2E), 100°C earlier compared with the control sample. Moreover, as the temperature increased gradually to 400°C, the CTSe phase obviously enhanced, accompanied by the appearance of the CZTSSe phase. This difference between the control and target samples is more clearly observed by quantifying the Raman intensities of different

Please cite this article in press as: Jiao et al., Suppressing defects in kesterite solar cells via balanced phase evolution to enable 15.1% certified record efficiency, Joule (2026), https://doi.org/10.1016/j.joule.2026.102345

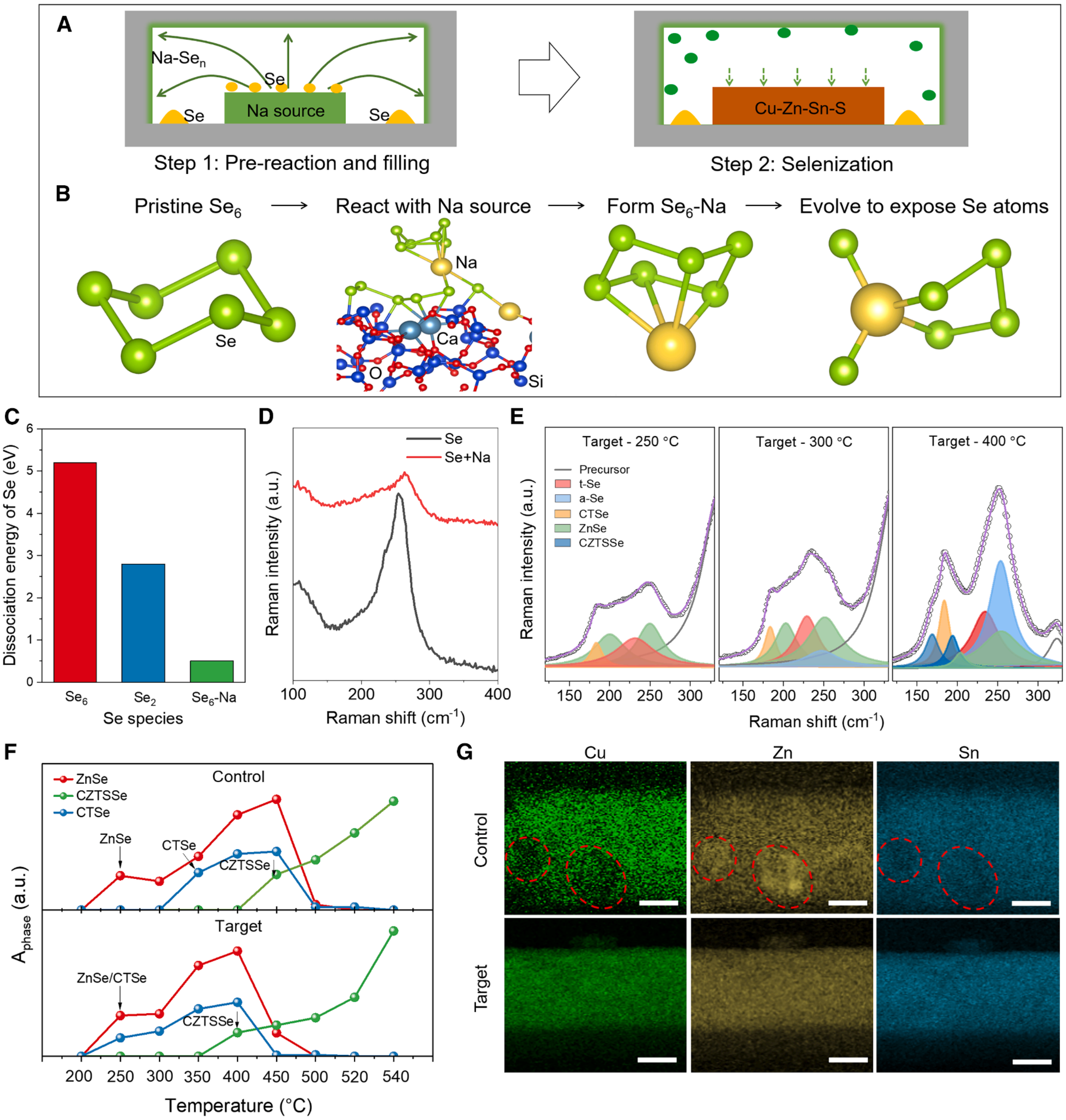

Figure 2. Activated selenization to balance the phase evolution

(A) Schematic diagram of our developed selenization activation strategy. In this strategy, Se is pre-reacted with a Na source (such as SLG) in the graphite box (the structure is shown in Figure S3), which is then used for subsequent film selenization.

(B) Evolution of molecular structures of Se when it reacts with the Na source. These structures were obtained using AIMD.

(C) Energy needed for a Se atom dissociation from different Se species.

(D) Raman spectra of Se species adsorbed in the graphite box with or without using the selenization activation strategy.

(E) Raman spectra of films selenized at varied temperatures based on Cu-Zn-Sn precursors and using the selenization activation strategy (target). Different phases were distinguished via multiple Lorentz-type peak fittings.

(F) Evolution of the Raman intensity of different phases with selenization temperature. The arrows depict the temperature point for the appearance of a certain phase.

(G) Cross-sectional SEM-EDX mapping images of the CZTSSe films selenization at 540°C for 15 s with (target) or without (control) using the selenization activation strategy. Scale bar: 1 μm.

phases (relative to the residual precursor phase) as a function of selenization temperature (Figure S9). As shown in Figure 2F, in the target sample, with the emergence of the CZTSSe phase at 400°C, the CTSe and ZnSe phases simultaneously and obviously decreased at 450°C, and almost disappeared at 500°C. In contrast, the CTSe and ZnSe phases in the control sample began to decrease only at 500°C, with the CTSe phase still observable at 520°C. These phenomena indicate that the

Please cite this article in press as: Jiao et al., Suppressing defects in kesterite solar cells via balanced phase evolution to enable 15.1% certified record efficiency, Joule (2026), https://doi.org/10.1016/j.joule.2026.102345

Na-Se species have indeed balanced the evolution of CTSe and ZnSe phases and promoted their transformation to the CZTSSe phase. The evolution of the XRD patterns of the CZTSSe films also exhibited a promoted selenization process (Figure S10).

This balanced phase evolution, particularly the earlier formation of the CTSe phase, effectively reduced the accumulation and segregation of ZnSe in the film. As in the cross-sectional SEM-EDX mapping images (Figure 2G), Cu, Zn, and Sn homogeneously distribute in the target sample, whereas the accumulation of Zn element can be obviously seen in the scale of micrometers in the control sample. In the final target, the CZTSSe film, a significant suppression in the Zn accumulation was also observed (Figure S11). It is evident that the inhibition of Zn segregation can promote more efficient incorporation of Zn into the final CZTSSe lattice, which in turn mitigates the formation of Cu_{Zn} and Sn_{Zn} defects.

Defect and photoelectric characterization

We employed thermal admittance spectroscopy (TAS) to characterize the defect properties of these two CZTSSe absorbers (Figures 3A and 3B; Figure S12).[36,37] The Cu_{Zn} defect was clearly detected in both samples, with an ionization energy at about 100–150 meV.[38,39] The difference primarily lies in the defect concentration and attempt-to-escape frequency (ν_0). As shown in Figures 3A and 3B, in the target sample, the defect concentration was reduced from 1.05×10^{16} to 4.12×10^{15} cm^{-3}, and the ν_0, which represents the charge-capturing activity, was decreased by two orders of magnitude, from 1.8×10^{10} s^{-1} to 1.9×10^{8} s^{-1}. This significant reduction in ν_0 implies that the ordering degree of the CZTSSe lattice has been effectively enhanced, leading to a significant suppression of the charge-capturing activity of all defects. In addition, since Cu_{Zn} and Sn_{Zn} defects share similar formation pathways,[11] the reduction in Cu_{Zn} defect concentration implies a corresponding decrease in Sn_{Zn} defects. In Raman spectra, an obvious decrease in the spectral intensity around 185 cm^{-1} and 220–250 cm^{-1} regions in the target sample provided more evidence from lattice vibration characteristics supporting the reduction in Cu_{Zn} and Sn_{Zn} defects (Figure 3C).[40–42]

The steady-state photoluminescence (PL) spectra, in which the target sample exhibited a much smaller red shift in photon emission (Figure 3D), demonstrated that reductions in both shallow and deep defects have suppressed bandgap and electrostatic potential fluctuations in CZTSSe.[9,43,44] The temperature-dependent V_{OC} measurement also supported this result.[45] The charge recombination activation energy (E_A, Note S1) of the target cell is nearly identical to its band gap (E_g), whereas that of the control cell is ~150 meV lower than its E_g (Figure 3E; Figure S13). The reduction in both defect concentration and charge-capturing activity also suppressed charge recombination in the CZTSSe film and corresponding solar cells. The target sample exhibited much slower PL decay, with a carrier lifetime reaching 535 ns (40 K), whereas the control sample only had a carrier lifetime of 226 ns (Figure S14). When in the cell, the target sample exhibited a much slower photovoltage decay, especially at high bias voltages (Figure 3F). Under 0 V bias, the target cell demonstrated an approximately single-exponential photovoltage decay, whereas the control cell exhibited a significant initial photovoltage decline, correlated with rapid charge recombination.[46,47] These findings suggest that balanced phase evolution has effectively mitigated defect formation and the corresponding charge non-radiative recombination losses in the CZTSSe absorbers.

We further employed modulated photocurrent methods to investigate the charge-transport properties of cells based on these two CZTSSe absorbers (Figures 3G and 3H).[46,47] For the control sample, when increasing the bias voltage from −500 mV to 500 mV, the peak intensity of photocurrent obviously decreased and the originally sharp photocurrent peak progressively transformed into a broader, dome-shaped profile, along with a continuous temporal shift of the peak toward longer times. In contrast, the target cell exhibited a consistently sharp photocurrent response, with the peak remaining temporally stable. These observations confirmed that the target sample has much better and more stable charge-transport capabilities across varied operational conditions. The suppression of defects and correlated band gap and electrostatic potential fluctuation is an important reason for this result. Additionally, the accelerated formation of the CZTSSe phase and the enhanced adsorption of Se in the films have improved crystallization growth of the target sample (Figure S15), which also contributed to the better charge transport (Figure S16).[17,48–51] Due to these benefits, the target cell exhibited a much stronger and more uniform electroluminescence (Figure 3I; Figure S17), which is a characteristic commonly associated with higher photovoltaic conversion performance.

Device performance characterization

We further characterized the photoelectric conversion performance of the cells based on these CZTSSe absorbers, and the statistical results are shown in Figure 4A. More detailed optimization processes are shown in Figures S19–S27. Through this strategy and synergistic optimization, the average PCE has improved from ~13.5% to ~15% with significant enhancements in the short-circuit current density (J_{SC}) and fill factor (FF). The J_{SC} increase is primarily due to the smaller E_g of the target CZTSSe absorber induced by the more complete selenization. Although the V_{OC} of the cell increased by only a few mV, the significant difference in the E_g between the control and target CZTSSe still indicated that the V_{OC} deficit (E_g/e-V_{OC}) of the target cell was significantly reduced by at least 40 mV. This result is primarily benefited from the suppression of defects and non-radiative charge recombination in CZTSSe. The impressively increased FF, with an average value from 0.7 to 0.74, is also strong evidence of the reduced defects and significantly improved charge-transport ability.

With these benefits, the PCE of the champion target cell reached 15.5% with J_{SC} of 38.8 mA cm^{-2}, V_{OC} of 0.53 V, and FF of 0.754 (Figure 4B), obviously surpassing that of the control cell with PCE of 14.0%. We also carried out performance tracking of the target cell at the maximum power point for 300 s. As shown in Figure 4C, when biased at 434.1 mV, the cell can give a steady-state current density output of 35.7 mA cm^{-2}, confirming a steady-state PCE of 15.5%. We also sent a target cell to an accredited independent laboratory (National PV Industry Measurement and Testing Center, China) for certification, which confirmed a PCE of 15.1% (Figure 4D; Figure S28),

Please cite this article in press as: Jiao et al., Suppressing defects in kesterite solar cells via balanced phase evolution to enable 15.1% certified record efficiency, Joule (2026), https://doi.org/10.1016/j.joule.2026.102345

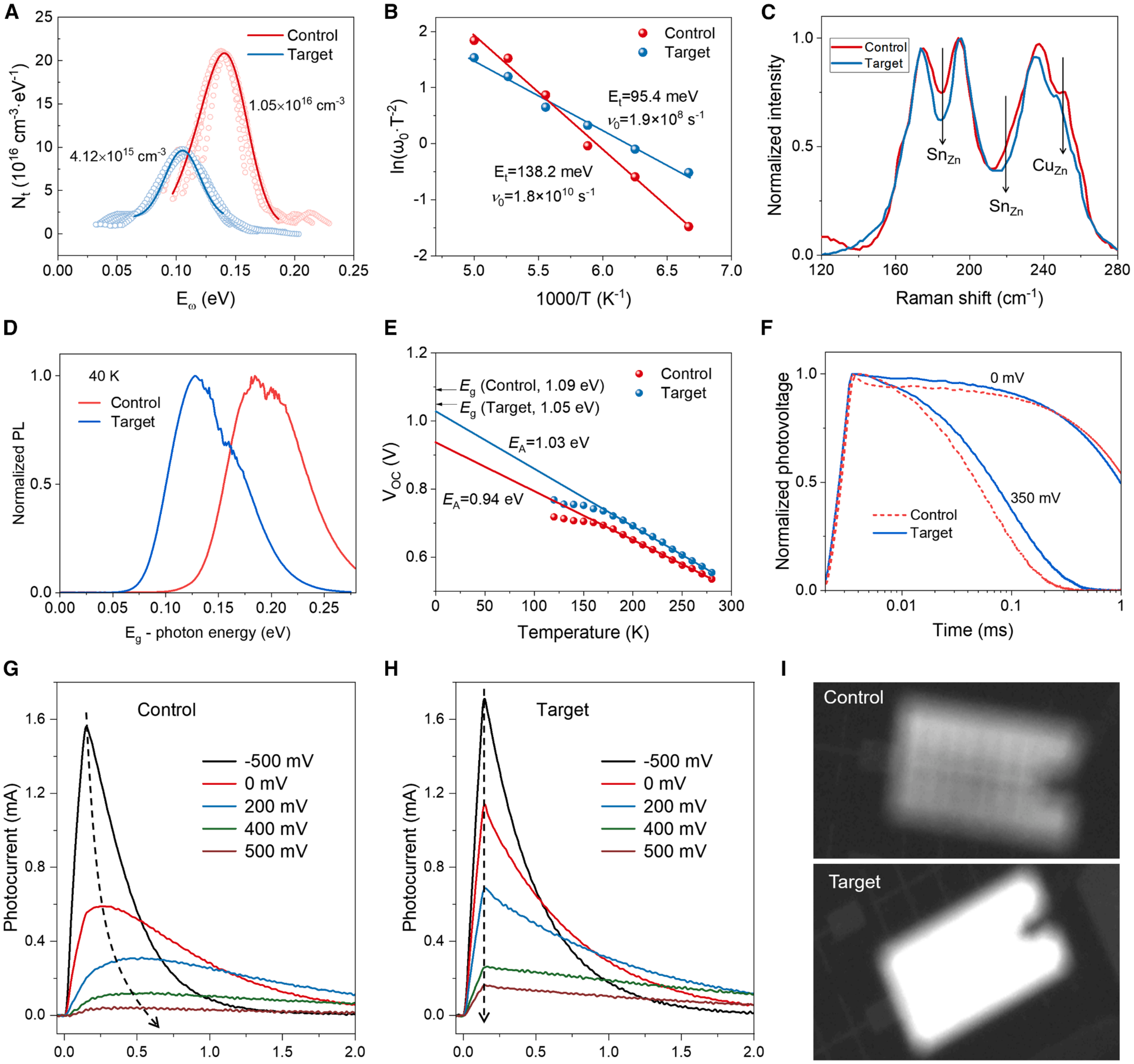

Figure 3. Defect and charge dynamics characterization

(A and B) (A) The energetic distribution of defects (Gaussian-type) and (B) Arrhenius plots of the defect charge capturing derived from thermal admittance spectra.

(C) Raman spectra of the final CZTSSe films. The arrows depict the spectral difference between these two samples and the correlated defects.

(D) Steady-state photoluminescence (PL) of CZTSSe absorbers measured at 40 K.

(E) Temperature-dependent V_{OC} of the cells. E_g represents the band gap of CZTSSe absorbers. The charge recombination activation energy (E_A) is obtained by extrapolating the linear region of V_{OC} to 0 K (Note S1).

(F) Photovoltage decay of the control and target cells.

(G and H) Photocurrent decay of the cells under varied bias voltages. The dashed lines show the evolution of photocurrent peaks with the voltage.

(I) Electroluminescence images of control and target cells under 600 mV.

thus representing a breakthrough beyond the commercialization threshold (15%) for solar cells. The external quantum efficiency of the cell gave an integral J_{SC} of 40.3 mA cm^{-2} and effective E_g of 1.05 eV (Figure 4E), indicating that the V_{OC} deficit of the cell has been reduced to 0.52 V. We further compared the performance parameters of the cell to their Shockley-Queisser (SQ) theoretical limits. The V_{OC}FF/V_{OC}^{SQ}FF^{SQ} value of our cell reaches 0.56, which surpasses that of all previously reported record cells and is the first one to exceed 0.55 (Figure 4F).[11,25,52–55] In terms of J_{SC}/J_{SC}^{SQ}, our cell also exhibits a significant

Please cite this article in press as: Jiao et al., Suppressing defects in kesterite solar cells via balanced phase evolution to enable 15.1% certified record efficiency, Joule (2026), https://doi.org/10.1016/j.joule.2026.102345

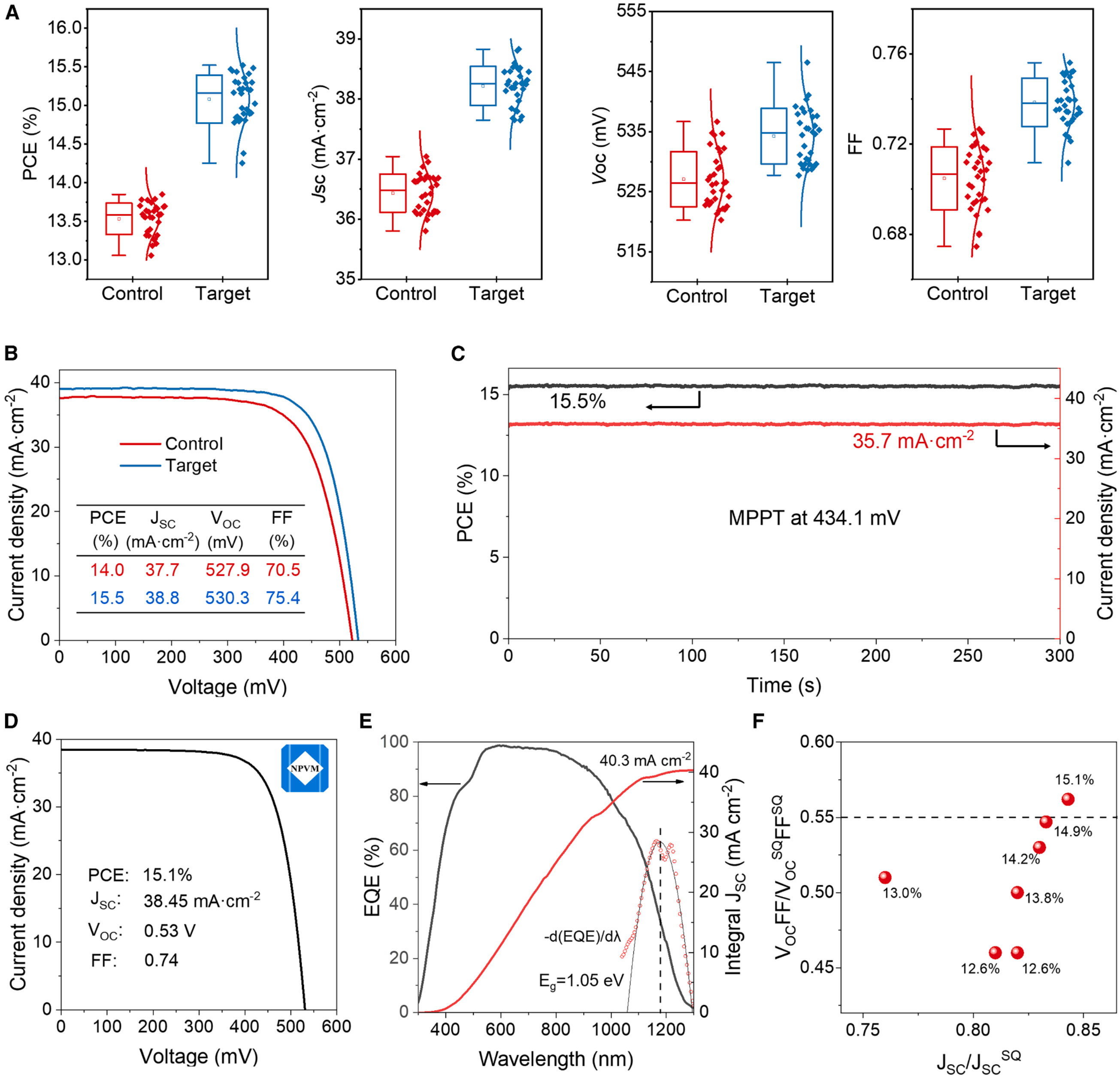

Figure 4. Device performance

(A) Statistical results of the photoelectric conversion performance of the control and target cells.

(B) Current density-voltage characteristics of the champion control and target cells.

(C) Maximum power point tracking (MPPT) of the target cell at 434.1 mV for 300 s. The cell gave a steady-state current density of 35.7 mA cm^{-2} and a corresponding PCE of 15.5%.

(D) Certified current density-voltage curve of the target cell, yielding PCE of 15.1%.

(E) EQE spectrum and corresponding current integration of the certified cell. The dashed vertical line depicts the positions of the absolute maxima of the differential EQE spectrum, corresponding to an E_g of 1.05 eV.

(F) Comparison of the performance parameters of record solar cells over the past several years with their SQ theoretical limits.[11,25,52–55]

improvement, primarily attributed to the improved optical properties of the device, including a thinned buffer/window layer and an enhanced long-wavelength response. Overall, our results exhibit substantial progress in key photovoltaic performance metrics of kesterite solar cells.

Moreover, our strategy focuses on the crystallization of the kesterite light-absorbing layer itself and therefore should be applicable to different types of kesterite solar cells, such as more environmentally friendly low-Cd or Cd-free cells or wide-bandgap pure-sulfide kesterite cells.[14,56–61] Looking ahead,

Please cite this article in press as: Jiao et al., Suppressing defects in kesterite solar cells via balanced phase evolution to enable 15.1% certified record efficiency, Joule (2026), https://doi.org/10.1016/j.joule.2026.102345

these diverse strategies for material regulation and device engineering—particularly those aimed at further minimizing the use of toxic Cd—will open up greater opportunities for the commercialization of kesterite solar cells.

Conclusion

In summary, this study elucidates that the delayed formation of CTSe relative to ZnSe during the phase evolution of the Cu-Zn-Sn-Se multinary system plays a critical role in causing defect formation in CZTSSe photovoltaic materials. To address this, a sodium-activated selenization strategy was developed, wherein pre-constructed Na-Se$_x$ species with highly reactive Se atoms were introduced to accelerate CTSe formation at reduced temperatures. This approach facilitated the synchronized coevolution of ZnSe and CTSe intermediates, promoting their conversion into the kesterite phase so as to suppress the generation of Zn-related defects. Consequently, this strategy enabled us to realize a certified PCE of >15% in CZTSSe solar cells, accompanied by a marked reduction in non-radiative voltage losses. This advancement not only overcomes a long-standing efficiency bottleneck for kesterite photovoltaics but also establishes a kinetic modulation paradigm for defect suppression in multinary chalcogenides. The findings underscore the necessity of crystallographic pathway engineering during thin-film synthesis and provide actionable insights for advancing the performance and scalability of emerging inorganic solar cell technologies.

METHODS

Materials

CuCl (99.999%, Alfa), Zn(Ac)$_2$ (99.99%, Aladdin), SnCl$_4$ (99.998%, Macklin), AgCl (99.5%, Innochem), CdCl$_2$ (99.99%, Aladdin), 2-methoxyethanol (99.8%, Aladdin), thiourea (99.99%, Aladdin, recrystallized before using), LiCl (99.9%, Alfa), NaCl (99.998%, Alfa), KCl (99.997%, Alfa), Se pellets (99.999%, Zhong Nuo Advanced Material), CdSO4·8/3 H$_2$O (99.99%, Aladdin), ammonium chloride ($\geq$ 99.5%, Sinopharm Chemical Reagent Co. Ltd.) and ammonia (25.0%–28.0%, Sinopharm Chemical Reagent Co. Ltd.) were used in this work. These chemicals, except thiourea, were used directly without further purification.

Precursor solution and film preparation

The precursor solution was prepared as follows: firstly, thiourea was dissolved in 2-methoxyethanol (MOE), followed by the addition of CuCl, which was then dissolved with stirring at 50°C to yield a colorless solution. Subsequently, AgCl was introduced into this solution and stirred for 1 h to obtain solution 1. Secondly, the MOE was added to a bottle containing SnCl$_4$ to produce a colorless solution. Zn(Ac)$_2$ and CdCl$_2$ were then dissolved in the Sn-containing solution to form solution 2. Thirdly, solutions 1 and 2 were mixed to give the final precursor solution. In the precursor solution, the concentrations of metal elements and thiourea are 1.88 M and 3.20 M, respectively. The molar ratios of (Ag + Cu)/(Zn + Cd + Sn), (Zn + Cd)/Sn, Ag/(Ag + Cu), Cd/(Cd + Zn), and thiourea/metal are 0.75, 1.12, 0.10, 0.06, and 1.7, respectively.

The Na-containing precursor solutions were prepared by adding NaCl to the aforementioned precursor solution, with concentrations of 25, 50, and 75 mmol/L, respectively.

The Kesterite precursor films were prepared by spin-coating the precursor solution on cleaned Mo substrates, followed by annealing on a 280°C hot plate in the air. The coating and annealing procedures were iteratively performed to achieve a target thickness of ~2 μm for the precursor films.

Pre-reaction and selenization

The Se pellets and SLG (or LiCl, NaCl, KCl) were placed into a graphite box and annealed at 545°C for 20 min under a nitrogen atmosphere using a rapid thermal processing (RTP) furnace. For SLGs, they were placed directly on the bottom of the graphite box, and for NaCl powders, they were placed in a quartz boat in the center of the graphite box. After the pre-filling process, the SLGs or salt powders/quartz boat were completely removed. Subsequently, the precursor film was placed into the same graphite box for a selenization treatment at the same temperature (545°C) under nitrogen for another 20 min, completing the absorbers preparation process. In both the pre-filling and selenization processes, nine Se pellets (~0.6 g) were used. After the film's selenization, the graphite box is cleaned by annealing at about 550°C under N$_2$ flow conditions for ~1 h. The above procedures are repeated for the next batch of CZTSSe film preparation.

Device fabrication

A 40~50 nm thickness CdS buffer layer was deposited on the top of CZTSSe films by the chemical bath deposition (CBD) method, followed by sputtering 50 nm i-ZnO layer (sputtering power: 55 W, gas source: Ar, pressure: ~2 Pa, temperature: 60°C) and 200 nm ITO layer (sputtering power: 60 W, gas source: Ar, pressure: ~0.2 Pa, temperature: 160°C). The Ni/Al grid electrode and ~110 nm MgF$_2$ anti-reflective coating were then deposited through thermal evaporation. The cells were separated from each other by mechanical scribing, and the designed area of an individual cell is 0.28 cm^2 (4×7 mm^2).

Characterization

Raman spectroscopy was conducted using a LabRAM HR Evolution (HORIBA) spectrometer with 532 and 325 nm lasers as the excitation sources. The adsorbed Na and Se content within the graphite box was quantitatively analyzed using inductively coupled plasma atomic emission spectroscopy (ICP-AES). SEM images were measured on a Hitachi S4800. STEM images were measured on FEI Tecnai G2 F30. Steady-state PL spectra were obtained with a PL spectrometer (Edinburgh Instruments, FLS 920), excited with a picosecond pulsed diode laser (EPL-640) with a wavelength of 638.2 nm while cooling down with liquid helium.

The *J-V* characteristics of the photovoltaic cells were measured using a Keithley 2601 Source Meter under simulated AM 1.5G solar illumination at an intensity of 100 mW·cm^{-2}. Calibration was performed using a silicon reference cell, which was calibrated by the National Institute of Metrology of China. The voltage sweep ranged from -50 to 600 mV at a scan rate of ~90 mV·s^{-1}. Cell certification was performed at the NPVM,

Please cite this article in press as: Jiao et al., Suppressing defects in kesterite solar cells via balanced phase evolution to enable 15.1% certified record efficiency, Joule (2026), https://doi.org/10.1016/j.joule.2026.102345

confirming a certified aperture area of 0.2697 cm^2 for the cell. All measurements were conducted under ambient conditions (air, 25°C, uncontrolled humidity), with no preconditioning steps prior to the measurements. The external quantum efficiency (EQE) was determined using an Enlitech QE-R system, which employed calibrated silicon (Si) and germanium (Ge) diodes for reference. Frequency-dependent admittance/capacitance spectra were acquired using a Princeton Versa STAT3 electrochemical workstation in the absence of illumination, with a scanning frequency ranging from 0.1 to 10^6 Hz. The temperature of the cell was meticulously regulated by a Lakeshore TTPX low-temperature probe station. C-V profiles, DLCP, TAS, and temperature-dependent *J-V* characteristics were all measured utilizing the Princeton Versa STAT3 electrochemical workstation. Modulated transient photocurrent and photovoltage (M-TPC/TPV) measurements were obtained by a tunable nanosecond laser pumped at 640 nm and recorded by a sub-nanosecond-resolved digital oscilloscope (Tektronix, DPO 7104) with a sampling resistance of 50 Ω or 1 MΩ. EL characterization was performed using a vis-NIR CMOS camera (Spark-Opt, CIS-CM990) covering a spectral range of 400–1700 nm.

Theoretical calculations

AIMD simulations were conducted using the Cambridge serial total energy package (CASTEP)[61] code, in which a plane wave basis set was used. The exchange-correlation interactions were modeled using the generalized gradient approximation (GGA) and the Perdew-Burke-Ernzerhof (PBE)[62] functional. Grimme's semi-empirical DFT-D[63] was introduced in the computations to guarantee a better description of the electron interaction in a long range. The Vanderbilt ultrasoft pseudopotential[64] was used with a cutoff energy of 400 eV. Geometric convergence tolerances were set for a maximum force of 0.03 eV/Å, a maximum energy change of 10^{-5} eV/atom, a maximum displacement of 0.001Å, and a maximum stress of 0.5 GPa.

Se_6 adsorption and Reactions on $NaCaSiO_2$ surfaces: Two gaseous Se_6 molecules were placed above the $NaCaSiO_2$ surface. AIMD simulations utilized identical time steps and gamma-point sampling. The temperature was maintained at 823 K using the Nosé-Hoover thermostat to observe dynamic adsorption behavior and interfacial interactions. Structural evolution, including Na-O bond weakening and Se_6-Na coordination, was observed over the simulation period.

Structural evolution of $NaSe_6$: AIMD simulations of the $NaSe_6$ molecule in the gas phase were performed at 823 K to investigate its thermal structural evolution behavior. A time step of 1.0 fs was used, and the Brillouin zone was sampled at the Γ-point without symmetric constraints. The simulation box dimensions were set to ensure negligible interactions between periodic images. Temperature control was achieved using the Nosé-Hoover thermostat with a Nosé mass parameter of 0.1. Each simulation was run for a total of 90 ps to capture the structural evolution dynamics.

Influence of N_2 molecules on $NaCaSiO_2$ Surface: To investigate the interaction of N_2 with the $NaCaSiO_2$ surface in the absence of Se_6, AIMD simulations were performed for a system containing the $NaCaSiO_2$ surface and four N_2 molecules at 823 K. The same surface model and simulation parameters as in Case 2 were employed, with the addition of four N_2 molecules placed over the $NaCaSiO_2$ surface. The total simulation time was 13 ps. No strong interactions between N_2 molecules and surface Na atoms were observed over the course of the simulation, indicating minimal reactivity of N_2 with the $NaCaSiO_2$ surface under these conditions.

All simulations explicitly avoided spin polarization to prioritize computational efficiency while retaining essential electronic interactions.

RESOURCE AVAILABILITY

Lead contact

Requests for further information and resources should be directed to and will be fulfilled by the lead contact, Qingbo Meng (qbmeng@iphy.ac.cn).

Materials availability

This study did not generate new unique reagents.

Data and code availability

All data reported in this paper will be shared by the lead contact upon request.

ACKNOWLEDGMENTS

This work was supported by the National Key R&D Program of China (2024YFB4205000), the National Natural Science Foundation of China (52222212, 52227803, 52502322, 52402243, and 52172261), the China National Postdoctoral Program for Innovative Talents (BX20250177), and the Zhejiang Provincial Natural Science Foundation (LQN25E020011). J.S. also gratefully acknowledges the support from the Youth Innovation Promotion Association of the Chinese Academy of Sciences (2022006).

AUTHOR CONTRIBUTIONS

M.J., J.S., and Q.M. conceived the idea and designed the experiments. M.J. and B.Z. did experiments and data analysis. Jinlin Wang and X.X. participated in improving cell performance and conducting characterization. T.G., S.C., Jingchen Wang, and Yuan Li supported CZTSSe solar cell fabrication. Yiming Li participated in microstructure and photoelectric characterization. H.W., Y. Luo, and D.L. supported the discussion. M.J., J.S., and Q.M. participated in writing the manuscript. All authors discussed the results and approved the manuscript.

DECLARATION OF INTERESTS

The authors declare no competing interests.

SUPPLEMENTAL INFORMATION

Supplemental information can be found online at https://doi.org/10.1016/j.joule.2026.102345.

Received: September 8, 2025
Revised: November 26, 2025
Accepted: January 26, 2026

REFERENCES

1. Park, J.S., Kim, S., Xie, Z., and Walsh, A. (2018). Point defect engineering in thin-film solar cells. Nat. Rev. Mater. *3*, 194–210. https://doi.org/10.1038/s41578-018-0026-7.

2. Polman, A., Knight, M., Garnett, E.C., Ehrler, B., and Sinke, W.C. (2016). Photovoltaic materials: Present efficiencies and future challenges. Science *352*, aad4424. https://doi.org/10.1126/science.aad4424.
3. Romero, M.J., Du, H., Teeter, G., Yan, Y., and Al-Jassim, M.M. (2011). Comparative study of the luminescence and intrinsic point defects in the kesterite Cu2ZnSnS4 and chalcopyrite Cu(In,Ga)Se_2 thin films used in photovoltaic applications. Phys. Rev., B *84*, 165324. https://doi.org/10.1103/PhysRevB.84.165324.
4. Neuschitzer, M., Sanchez, Y., Olar, T., Thersleff, T., Lopez-Marino, S., Oliva, F., Espindola-Rodriguez, M., Xie, H., Placidi, M., Izquierdo-Roca, V., et al. (2015). Complex Surface Chemistry of Kesterites: Cu/Zn Reordering after Low Temperature Postdeposition Annealing and Its Role in High Performance Devices. Chem. Mater. *27*, 5279–5287. https://doi.org/10.1021/acs.chemmater.5b01473.
5. Larramona, G., Levcenko, S., Bourdais, S., Jacob, A., Choné, C., Delatouche, B., Moisan, C., Just, J., Unold, T., and Dennler, G. (2015). Fine-Tuning the Sn Content in CZTSSe Thin Films to Achieve 10.8% Solar Cell Efficiency from Spray-Deposited Water–Ethanol-Based Colloidal Inks. Adv. Energy Mater. *5*, 1501404. https://doi.org/10.1002/aenm.201501404.
6. Kumar, M., Dubey, A., Adhikari, N., Venkatesan, S., and Qiao, Q. (2015). Strategic review of secondary phases, defects and defect-complexes in kesterite CZTS–Se solar cells. Energy Environ. Sci. *8*, 3134–3159. https://doi.org/10.1039/C5EE02153G.
7. Chen, S., Yang, J.H., Gong, X.G., Walsh, A., and Wei, S.H. (2010). Intrinsic point defects and complexes in the quaternary kesterite semiconductor Cu_2ZnSnS_4. Phys. Rev., B *81*, 245204. https://doi.org/10.1103/PhysRevB.81.245204.
8. Chen, S., Walsh, A., Gong, X.G., and Wei, S.H. (2013). Classification of Lattice Defects in the Kesterite Cu_2ZnSnS_4 and $Cu_2ZnSnSe_4$ Earth-Abundant Solar Cell Absorbers. Adv. Mater. *25*, 1522–1539. https://doi.org/10.1002/adma.201203146.
9. Bourdais, S., Choné, C., Delatouche, B., Jacob, A., Larramona, G., Moisan, C., Lafond, A., Donatini, F., Rey, G., Siebentritt, S., et al. (2016). Is the Cu/Zn Disorder the Main Culprit for the Voltage Deficit in Kesterite Solar Cells? Adv. Energy Mater. *6*, 1502276. https://doi.org/10.1002/aenm.201502276.
10. Gong, Y., Zhang, Y., Zhu, Q., Zhou, Y., Qiu, R., Niu, C., Yan, W., Huang, W., and Xin, H. (2021). Identifying the origin of the V_{OC} deficit of kesterite solar cells from the two grain growth mechanisms induced by Sn^{2+} and Sn^{4+} precursors in DMSO solution. Energy Environ. Sci. *14*, 2369–2380. https://doi.org/10.1039/D0EE03702H.
11. Shi, J., Wang, J., Meng, F., Zhou, J., Xu, X., Yin, K., Lou, L., Jiao, M., Zhang, B., Wu, H., et al. (2024). Multinary alloying for facilitated cation exchange and suppressed defect formation in kesterite solar cells with above 14% certified efficiency. Nat. Energy *9*, 1095–1104. https://doi.org/10.1038/s41560-024-01551-5.
12. Giraldo, S., Saucedo, E., Neuschitzer, M., Oliva, F., Placidi, M., Alcobé, X., Izquierdo-Roca, V., Kim, S., Tampo, H., Shibata, H., et al. (2018). How small amounts of Ge modify the formation pathways and crystallization of kesterites. Energy Environ. Sci. *11*, 582–593. https://doi.org/10.1039/C7EE02318A.
13. Altamura, G., and Vidal, J. (2016). Impact of Minor Phases on the Performances of CZTSSe Thin-Film Solar Cells. Chem. Mater. *28*, 3540–3563. https://doi.org/10.1021/acs.chemmater.6b00069.
14. Wang, A., Huang, J., Cong, J., Yuan, X., He, M., Li, J., Yan, C., Cui, X., Song, N., Zhou, S., et al. (2023). Cd-Free Pure Sulfide Kesterite Cu_2ZnSnS_4 Solar Cell with Over 800 mV Open-Circuit Voltage Enabled by Phase Evolution Intervention. Adv. Mater. *36*, 2307733. https://doi.org/10.1002/adma.202307733.
15. Hsu, W.C., Bob, B., Yang, W., Chung, C.H., and Yang, Y. (2012). Reaction pathways for the formation of $Cu_2ZnSn(Se,S)_4$ absorber materials from liquid-phase hydrazine-based precursor inks. Energy Environ. Sci. *5*, 8564. https://doi.org/10.1039/c2ee21529b.
16. Yin, X., Tang, C., Sun, L., Shen, Z., and Gong, H. (2014). Study on Phase Formation Mechanism of Non- and Near-Stoichiometric $Cu_2ZnSn(S,Se)_4$ Film Prepared by Selenization of Cu–Sn–Zn–S Precursors. Chem. Mater. *26*, 2005–2014. https://doi.org/10.1021/cm403423e.
17. Hages, C.J., Koeper, M.J., Miskin, C.K., Brew, K.W., and Agrawal, R. (2016). Controlled Grain Growth for High Performance Nanoparticle-Based Kesterite Solar Cells. Chem. Mater. *28*, 7703–7714. https://doi.org/10.1021/acs.chemmater.6b02733.
18. Jian, Y., Zhao, Y., Zhao, J., Chen, S., Su, Z., Ma, H., Zhang, X., and Liang, G. (2025). Controllable SnS-Vapor-Assisted Selenization to Enhance Carrier Transport for Highly Efficient Kesterite Solar Cells. Adv. Energy Mater. *15*, e04071. https://doi.org/10.1002/aenm.202504071.
19. Gong, Y., Zhang, Y., Jedlicka, E., Giridharagopal, R., Clark, J.A., Yan, W., Niu, C., Qiu, R., Jiang, J., Yu, S., et al. (2020). Sn^{4+} precursor enables 12.4% efficient kesterite solar cell from DMSO solution with open circuit voltage deficit below 0.30 V. Sci. China Mater. *64*, 52–60. https://doi.org/10.1007/s40843-020-1408-x.
20. Cong, J., He, M., Jang, J.S., Huang, J., Privat, K., Chen, Y.-S., Li, J., Yang, L., Green, M.A., Kim, J.H., et al. (2024). Unveiling the Role of Ge in CZTSSe Solar Cells by Advanced Micro-To-Atom Scale Characterizations. Adv. Sci. (Weinh) *11*, e2305938. https://doi.org/10.1002/advs.202305938.
21. Mousel, M., Schwarz, T., Djemour, R., Weiss, T.P., Sendler, J., Malaquias, J.C., Redinger, A., Cojocaru-Mirédin, O., Choi, P.-P., and Siebentritt, S. (2013). Cu-Rich Precursors Improve Kesterite Solar Cells. Adv. Energy Mater. *4*, 1300543. https://doi.org/10.1002/aenm.201300543.
22. Timo Wätjen, J., Zimmermann, U., and Edoff, M. (2012). Microanalysis of post-deposition annealing of Cu(In,Ga)Se_2 solar cells. Sol. Energy Mater. Sol. Cells *107*, 396–402. https://doi.org/10.1016/j.solmat.2012.04.011.
23. Yang, W.C., Miskin, C.K., Hages, C.J., Hanley, E.C., Handwerker, C., Stach, E.A., and Agrawal, R. (2014). Kesterite $Cu_2ZnSn(S,Se)_4$ Absorbers Converted from Metastable, Wurtzite-Derived Cu_2ZnSnS_4 Nanoparticles. Chem. Mater. *26*, 3530–3534. https://doi.org/10.1021/cm501111z.
24. Xu, X., Zhou, J., Yin, K., Wang, J., Lou, L., Jiao, M., Zhang, B., Li, D., Shi, J., Wu, H., et al. (2023). Controlling Selenization Equilibrium Enables High-Quality Kesterite Absorbers for Efficient Solar Cells. Nat. Commun. *14*, 6650. https://doi.org/10.1038/s41467-023-42460-7.
25. Zhou, J., Xu, X., Wu, H., Wang, J., Lou, L., Yin, K., Gong, Y., Shi, J., Luo, Y., Li, D., et al. (2023). Control of the phase evolution of kesterite by tuning of the selenium partial pressure for solar cells with 13.8% certified efficiency. Nat. Energy *8*, 526–535. https://doi.org/10.1038/s41560-023-01251-6.
26. Chi, J., Wei, H., Chu, L., Han, L., Liu, T., Zhong, X., Kou, D., Zhou, W., Zhou, Z., Yuan, S., et al. (2025). Phase evolution regulation of CZTSSe absorbers via a ZnO blocking layer enables 14.45% efficient kesterite solar cells with low V_{OC} deficit. Energy Environ. Sci. *18*, 8366–8381. https://doi.org/10.1039/D5EE02706C.
27. Chen, Q., Bernardi, S., and Zhang, Y. (2017). Spatially Resolved Laser-Induced Modification Raman Spectroscopy for Probing the Microscopic Structural Variations in the Quaternary Alloy $Cu_2ZnSnSe_4$. Phys. Rev. Appl. *8*, 034008. https://doi.org/10.1103/PhysRevApplied.8.034008.
28. Fernandes, P.A., Sousa, M.G., Salomé, P.M.P., Leitão, J.P., and da Cunha, A.F. (2013). Thermodynamic pathway for the formation of SnSe and $SnSe_2$ polycrystalline thin films by selenization of metal precursors. CrystEngComm *15*, 10278. https://doi.org/10.1039/c3ce41537f.
29. Yannopoulos, S.N., and Andrikopoulos, K.S. (2004). Raman scattering study on structural and dynamical features of noncrystalline selenium. J. Chem. Phys. *121*, 4747–4758. https://doi.org/10.1063/1.1780151.
30. Berkowitz, J., and Chupka, W.A. (1966). Equilibrium Composition of Selenium Vapor; the Thermodynamics of the Vaporization of HgSe, CdSe, and SrSe. J. Chem. Phys. *45*, 4289–4302. https://doi.org/10.1063/1.1727488.
31. Cheng, H., DePuydt, J.M., Haase, M., and Potts, J.E. (1990). Low-temperature growth of ZnSe by molecular beam epitaxy using cracked selenium. Appl. Phys. Lett. *56*, 848–850. https://doi.org/10.1063/1.102681.

Please cite this article in press as: Jiao et al., Suppressing defects in kesterite solar cells via balanced phase evolution to enable 15.1% certified record efficiency, Joule (2026), https://doi.org/10.1016/j.joule.2026.102345

32. Ishizuka, S., Shibata, H., Yamada, A., Fons, P., Sakurai, K., Matsubara, K., and Niki, S. (2007). Growth of polycrystalline Cu(In,Ga)Se_2 thin films using a radio frequency-cracked Se-radical beam source and application for photovoltaic devices. Appl. Phys. Lett. *91*, 041902. https://doi.org/10.1063/1.2766669.
33. Ishizuka, S., Yamada, A., Shibata, H., Fons, P., Sakurai, K., Matsubara, K., and Niki, S. (2009). Large grain Cu(In,Ga)Se_2 thin film growth using a Se-radical beam source. Sol. Energy Mater. Sol. Cells *93*, 792–796. https://doi.org/10.1016/j.solmat.2008.09.043.
34. Kawamura, M., Fujita, T., Yamada, A., and Konagai, M. (2009). Cu(In,Ga)Se_2 thin-film solar cells grown with cracked selenium. J. Cryst. Growth *311*, 753–756. https://doi.org/10.1016/j.jcrysgro.2008.09.091.
35. Li, J., Wang, H., Wu, L., Chen, C., Zhou, Z., Liu, F., Sun, Y., Han, J., and Zhang, Y. (2016). Growth of $Cu_2ZnSnSe_4$ Film under Controllable Se Vapor Composition and Impact of Low Cu Content on Solar Cell Efficiency. ACS Appl. Mater. Interfaces *8*, 10283–10292. https://doi.org/10.1021/acsami.6b00081.
36. Tiwari, D., Yakushev, M.V., Koehler, T., Cattelan, M., Fox, N., Martin, R.W., Klenk, R., and Férmin, D.J. (2022). Mapping the Energetics of Defect States in Cu_2ZnSnS_4 films and the Impact of Sb Doping. ACS Appl. Energy Mater. *5*, 3933–3940. https://doi.org/10.1021/acsaem.1c03729.
37. Walter, T., Herberholz, R., Müller, C., and Schock, H.W. (1996). Determination of defect distributions from admittance measurements and application to Cu(In,Ga)Se_2 based heterojunctions. J. Appl. Phys. *80*, 4411–4420. https://doi.org/10.1063/1.363401.
38. Duan, H.S., Yang, W., Bob, B., Hsu, C.J., Lei, B., and Yang, Y. (2012). The Role of Sulfur in Solution-Processed $Cu_2ZnSn(S,Se)_4$ and its Effect on Defect Properties. Adv. Funct. Mater. *23*, 1466–1471. https://doi.org/10.1002/adfm.201201732.
39. Wang, J., Zhou, J., Xu, X., Meng, F., Xiang, C., Lou, L., Yin, K., Duan, B., Wu, H., Shi, J., et al. (2022). Ge Bidirectional Diffusion to Simultaneously Engineer Back Interface and Bulk Defects in the Absorber for Efficient CZTSSe Solar Cells. Adv. Mater. *34*, 2202858. https://doi.org/10.1002/adma.202202858.
40. Mortazavi Amiri, N.B., and Postnikov, A.V. (2010). Electronic structure and lattice dynamics in kesterite-type $Cu_2ZnSnSe_4$ from first-principles calculations. Phys. Rev., B *82*, 205204. https://doi.org/10.1103/PhysRevB.82.205204.
41. Dimitrievska, M., Fairbrother, A., Saucedo, E., Pérez-Rodríguez, A., and Izquierdo-Roca, V. (2015). Influence of compositionally induced defects on the vibrational properties of device grade $Cu_2ZnSnSe_4$ absorbers for kesterite based solar cells. Appl. Phys. Lett. *106*, 073903. https://doi.org/10.1063/1.4913262.
42. Redinger, A., Hönes, K., Fontané, X., Izquierdo-Roca, V., Saucedo, E., Valle, N., Pérez-Rodríguez, A., and Siebentritt, S. (2011). Detection of a ZnSe secondary phase in coevaporated $Cu_2ZnSnSe_4$ thin films. Appl. Phys. Lett. *98*, 101907. https://doi.org/10.1063/1.3558706.
43. Rey, G., Redinger, A., Sendler, J., Weiss, T.P., Thevenin, M., Guennou, M., El Adib, B., and Siebentritt, S. (2014). The band gap of $Cu_2ZnSnSe_4$: Effect of order-disorder. Appl. Phys. Lett. *105*, 112106. https://doi.org/10.1063/1.4896315.
44. Scragg, J.J.S., Choubrac, L., Lafond, A., Ericson, T., and Platzer-Björkman, C. (2014). A low-temperature order-disorder transition in Cu_2ZnSnS_4 thin films. Appl. Phys. Lett. *104*, 041911. https://doi.org/10.1063/1.4863685.
45. Lou, L., Wang, J., Yin, K., Meng, F., Xu, X., Zhou, J., Wu, H., Shi, J., Luo, Y., Li, D., et al. (2023). Crown Ether-Assisted Colloidal ZnO Window Layer Engineering for Efficient Kesterite $(Ag,Cu)_2ZnSn(S,Se)_4$ Solar Cells. ACS Energy Lett. *8*, 3775–3783. https://doi.org/10.1021/acsenergylett.3c01329.
46. Li, Y., Shi, J., Yu, B., Duan, B., Wu, J., Li, H., Li, D., Luo, Y., Wu, H., and Meng, Q. (2020). Exploiting Electrical Transients to Quantify Charge Loss in Solar Cells. Joule *4*, 472–489. https://doi.org/10.1016/j.joule.2019.12.016.
47. Shi, J., Li, D., Luo, Y., Wu, H., and Meng, Q. (2016). Opto-electro-modulated transient photovoltage and photocurrent system for investigation of charge transport and recombination in solar cells. Rev. Sci. Instrum. *87*, 123107. https://doi.org/10.1063/1.4972104.
48. Johnson, M., Baryshev, S.V., Thimsen, E., Manno, M., Zhang, X., Veryovkin, I.V., Leighton, C., and Aydil, E.S. (2014). Alkali-metal-enhanced grain growth in Cu_2ZnSnS_4 thin films. Energy Environ. Sci. *7*, 1931–1938. https://doi.org/10.1039/C3EE44130J.
49. Sutter-Fella, C.M., Stückelberger, J.A., Hagendorfer, H., La Mattina, F., Kranz, L., Nishiwaki, S., Uhl, A.R., Romanyuk, Y.E., and Tiwari, A.N. (2014). Sodium Assisted Sintering of Chalcogenides and Its Application to Solution Processed $Cu_2ZnSn(S,Se)_4$ Thin Film Solar Cells. Chem. Mater. *26*, 1420–1425. https://doi.org/10.1021/cm403504u.
50. Braunger, D., Hariskos, D., Bilger, G., Rau, U., and Schock, H.W. (2000). Influence of sodium on the growth of polycrystalline Cu(In,Ga)Se_2 thin films. Thin Solid Films *361–362*, 161–166. https://doi.org/10.1016/S0040-6090(99)00777-4.
51. Yuan, Z.K., Chen, S., Xie, Y., Park, J.S., Xiang, H., Gong, X.G., and Wei, S.H. (2016). Na-Diffusion Enhanced p-type Conductivity in Cu(In,Ga)Se_2: A New Mechanism for Efficient Doping in Semiconductors. Adv. Energy Mater. *6*, 1601191. https://doi.org/10.1002/aenm.201601191.
52. Gong, Y., Zhu, Q., Li, B., Wang, S., Duan, B., Lou, L., Xiang, C., Jedlicka, E., Giridharagopal, R., Zhou, Y., et al. (2022). Elemental de-mixing-induced epitaxial kesterite/CdS interface enabling 13%-efficiency kesterite solar cells. Nat. Energy *7*, 966–977. https://doi.org/10.1038/s41560-022-01132-4.
53. Son, D.H., Kim, S.H., Kim, S.Y., Kim, Y.I., Sim, J.H., Park, S.N., Jeon, D.H., Hwang, D.K., Sung, S.J., Kang, J.K., et al. (2019). Effect of solid-H_2S gas reactions on CZTSSe thin film growth and photovoltaic properties of a 12.62% efficiency device. J. Mater. Chem. A *7*, 25279–25289. https://doi.org/10.1039/C9TA08310C.
54. Wang, W., Winkler, M.T., Gunawan, O., Gokmen, T., Todorov, T.K., Zhu, Y., and Mitzi, D.B. (2013). Device Characteristics of CZTSSe Thin-Film Solar Cells with 12.6% Efficiency. Adv. Energy Mater. *4*, 1301465. https://doi.org/10.1002/aenm.201301465.
55. Wang, J., Meng, F., Lou, L., Yin, K., Xu, X., Jiao, M., Zhang, B., Li, Y., Shi, J., Wu, H., et al. (2026). Vacancy-enhanced cation ordering via magnesium doping to enable kesterite solar cells with 14.9% certified efficiency. Nat. Energy *11*, 66–75. https://doi.org/10.1038/s41560-025-01902-w.
56. Tseberlidis, G., Gobbo, C., Trifiletti, V., Di Palma, V., and Binetti, S. (2024). Cd-free kesterite solar cells: State-of-the-art and perspectives. Sustain. Mater. Technol. *41*, e01003. https://doi.org/10.1016/j.susmat.2024.e01003.
57. Platzer-Björkman, C., Barreau, N., Bär, M., Choubrac, L., Grenet, L., Heo, J., Kubart, T., Mittiga, A., Sanchez, Y., Scragg, J., et al. (2019). Back and front contacts in kesterite solar cells: state-of-the-art and open questions. J. Phys.: Energy *1*, 044005. https://doi.org/10.1088/2515-7655/ab3708.
58. Wang, A., He, M., Green, M.A., Sun, K., and Hao, X. (2023). A Critical Review on the Progress of Kesterite Solar Cells: Current Strategies and Insights. Adv. Energy Mater. *13*, 2203046. https://doi.org/10.1002/aenm.202203046.
59. Wu, T., Chen, S., Su, Z., Wang, Z., Luo, P., Zheng, Z., Luo, J., Ma, H., Zhang, X., and Liang, G. (2025). Heat treatment in an oxygen-rich environment to suppress deep-level traps in Cu_2ZnSnS_2 solar cell with 11.51% certified efficiency. Nat. Energy *10*, 630–640. https://doi.org/10.1038/s41560-025-01756-2.
60. Son, D.-H., Park, H.K., Kim, D.-H., Kang, J.-K., Sung, S.-J., Hwang, D.-K., Lee, J., Jeon, D.-H., Cho, Y., Jo, W., et al. (2024). Vertical plane depth-resolved surface potential and carrier separation characteristics in flexible CZTSSe solar cells with over 12% efficiency. Carbon Energy *6*, e434. https://doi.org/10.1002/cey2.434.

Please cite this article in press as: Jiao et al., Suppressing defects in kesterite solar cells via balanced phase evolution to enable 15.1% certified record efficiency, Joule (2026), https://doi.org/10.1016/j.joule.2026.102345

61. Segall, M.D., Lindan, P.J.D., Probert, M.J., Pickard, C.J., Hasnip, P.J., Clark, S.J., and Payne, M.C. (2002). First-principles simulation: ideas, illustrations and the CASTEP code. J. Phys.: Condens. Matter *14*, 2717–2744. https://doi.org/10.1088/0953-8984/14/11/301.

62. Perdew, J.P., Burke, K., and Ernzerhof, M. (1996). Generalized gradient approximation made simple. Phys. Rev. Lett. *77*, 3865–3868. https://doi.org/10.1103/PhysRevLett.77.3865.

63. Grimme, S., Antony, J., Ehrlich, S., and Krieg, H. (2010). A consistent and accurate ab initio parametrization of density functional dispersion correction (DFT-D) for the 94 elements H-Pu. J. Chem. Phys. *132*, 154104. https://doi.org/10.1063/1.3382344.

64. Vanderbilt, D. (1990). Soft self-consistent pseudopotentials in a generalized eigenvalue formalism. Phys. Rev. B Condens. Matter *41*, 7892–7895. https://doi.org/10.1103/PhysRevB.41.7892.